Ultramicroscopy 158 (2015) 98–104

Contents lists available at ScienceDirect

Ultramicroscopy

journal homepage: www.elsevier.com/locate/ultramic

High contrast 3D imaging of surfaces near the wavelength limit using tabletop EUV ptychography

Bosheng Zhang*, Dennis F. Gardner, Matthew D. Seaberg, Elisabeth R. Shanblatt, Henry C. Kapteyn, Margaret M. Murnane, Daniel E. Adams

JILA, University of Colorado, 440 UCB, Boulder, CO 80309-0440, USA

ARTICLE INFO

Article history:
Received 19 April 2015
Received in revised form
10 July 2015
Accepted 21 July 2015
Available online 22 July 2015

Keywords:
Coherent diffraction imaging
High harmonic generation
X-ray microscopy
Reflection mode
Surface profilometry

ABSTRACT

Scanning electron microscopy and atomic force microscopy are well-established techniques for imaging surfaces with nanometer resolution. Here we demonstrate a complementary and powerful approach based on tabletop extreme-ultraviolet ptychography that enables quantitative full field imaging with higher contrast than other techniques, and with compositional and topographical information. Using a high numerical aperture reflection-mode microscope illuminated by a tabletop 30 nm high harmonic source, we retrieve high quality, high contrast, full field images with 40 nm by 80 nm lateral resolution ($\approx 1.3\lambda$), with a total exposure time of less than 1 min. Finally, quantitative phase information enables surface profilometry with ultra-high, 6 Å axial resolution. In the future, this work will enable dynamic imaging of functioning nanosystems with unprecedented combined spatial (<10 nm) and temporal (<10 fs) resolution, in thick opaque samples, with elemental, chemical and magnetic sensitivity.

Microscopic imaging is critical for discovery and innovation in science and technology, accelerating advances in materials, bio, nano, and energy sciences, as well as nanoelectronics, data storage, and medicine. X-ray crystallography revolutionized many fields by determining crystalline structure on an atomic scale. Electron, X-ray, and scanning-probe microscopies can image complex matter with atomic-level spatial resolution. Super-resolved fluorescence microscopy can generate beautiful images of cellular organelles and structures. However, even these advanced imaging capabilities have limitations. Current imaging techniques are nowhere near their fundamental limits in terms of spatial and temporal resolution. Most techniques require extensive sample preparation, can damage the sample, are not applicable in situ, require invasive labeling, are chemically unspecific, or suffer from limited speed and field-of-view. Opaque, scattering, and disordered (non-crystalline) samples present a formidable challenge using any imaging modality.

Coherent diffractive imaging (CDI) is an important new full field imaging technique that can achieve very high spatial and temporal resolution simultaneously. In CDI, a spatially coherent beam illuminates an object, and the intensity of the scattered light is then collected on a pixel array detector. A generalized projection algorithm can then essentially replace any image-forming optics by solving for the complex-valued map of the sample that satisfies both the detector plane constraint (i.e. the magnitude of the retrieved scatter pattern must be consistent with the measured scattered pattern) and one or more a-priori sample plane constraints. The resulting image contains quantitative amplitude (material composition) and phase (thickness/height) contrast, providing more information about a surface or object than most traditional imaging techniques. Ptychography CDI has proven to be particularly robust when imaging objects containing complicated and/or large phase and amplitude variations [1–3]. This is because instead of collecting a single diffraction pattern as in traditional CDI, ptychography CDI acquires diffraction patterns from several adjacent overlapping positions. Although this requires that the sample be scanned, the resulting information redundancy from overlapping scatter patterns makes it possible to robustly and reliably solve the phase retrieval problem.

Coincident with the development of CDI, phase matching of the high harmonic generation (HHG) [4–9] process produces bright spatially coherent beams on a tabletop, spanning the entire VUV, EUV and soft X-ray regions of the spectrum, to photon energies >1.6 keV [9]. HHG takes advantage of the intense electric field created at the focus of a femtosecond laser that ionizes an atom and creates a nanoscale quantum antenna. Some laser driven electrons can acquire a large oscillation energy, which is then released in the form of an HHG photon after the electron recombines with the parent ion. HHG sources, when implemented in an optimal phase-matched geometry, can achieve full spatial and

* Corresponding author.
E-mail address: Bosheng.Zhang@colorado.edu (B. Zhang).

http://dx.doi.org/10.1016/j.ultramic.2015.07.006

temporal coherence, with attosecond to femtosecond pulse durations [10,11]. Recently, HHG sources have been successfully used to implement a variety of CDI techniques [12–18]. However, while EUV and X-ray CDI microscopy has been used for a wide range of applications, most experiments to date were performed in a transmission geometry. Although several attempts were made to apply CDI in reflection geometr [16,19–25] achieving high fidelity surface imaging comparable to scanning electron microscopy (SEM) [26–28] and atomic force microscopy (AFM) [29] in 3D has been challenging. In previous work [24], we demonstrated the first, general reflection mode result, working at an arbitrary angle of illumination and arbitrary angle of diffraction onto the detector however, in that work the numerical aperture was relatively low, (NA$\sim$0.1) resulting in a transverse resolution of 150 nm.

Here we demonstrate high contrast, high quality, full field 3D imaging of surfaces by combining a tabletop HHG source at a wavelength of 30 nm with high NA (NA=0.4) reflection mode ptychographic coherent diffraction imaging (CDI). We achieve record lateral spatial resolution of $\approx 1.3\lambda$ (40 nm), with 6 Å axial resolution. Our image quality compares very favorably with scanning electron microscopy (SEM) and atomic force microscopy (AFM), resulting in higher-contrast imaging with less sample damage. Moreover, the working distance is long at 3–10 cm. When combined with the femtosecond time resolution ($\approx$ 10 fs) and shorter wavelengths ($\approx$ 1–30 nm) readily available from HHG sources, [9] and in a pump-probe geometry to probe periodic phenomena, this work will make it possible to image the fastest charge, spin and phonon dynamics in functioning nanosystems in real space and time.

We note that compared to similar imaging techniques, EUV-based reflection CDI provides a powerful contrast mechanism by combining both material and geometric information. While zone plate based microscopes [30,31] can achieve $\approx$ 10–25 nm spatial resolution using shorter wavelength light, they result in amplitude-only images and thus contain less information about the object. Compared with AFM, where image contrast comes solely from height differences regardless of material properties, CDI derives its contrast from the reflected complex exit surface wave, which includes material dependent information. Finally, compared with SEM, which provides little information about height variation, the high phase contrast mechanism in reflection CDI inherently records even slight topographical features.

1. Experiment

To generate HHG beams, we focus ultrashort pulses from a Ti: sapphire laser amplifier system (central wavelength of 780 nm, pulse energy of 1.4 mJ, 5 kHz repetition rate and 22 fs pulse width) into a 200 μm diameter, 5 cm long, hollow waveguide filled with argon (36 Torr backing pressure). These experimental conditions are optimal for generating phase-matched, spatially coherent harmonics at wavelengths near 30 nm. After the waveguide, the CDI microscope is maintained at high vacuum ($\approx 10^{-6}$ Torr) to avoid absorption of the EUV light. We use a pair of silicon rejecter mirrors set near Brewster's angle for 780 nm, together with two 200 nm-thick aluminum filters, to completely eliminate the fundamental laser light. As shown in Fig. 1a, two 45° angle-of-incidence multilayer mirrors select the 27th harmonic (30 nm) which is then focused near the sample by an ellipsoidal nickel-coated mirror set at 5° grazing incidence. The beam then illuminates the sample at an angle of 50.5°, and has a slight negative phase curvature due to the position of the sample relative to the focus.

The sample consists of titanium shapes patterned with e-beam lithography onto a silicon substrate (SEM image shown in Fig. 1b). During the period after the sample was fabricated, surface contamination resulted in very fine height variations across the sample. To demonstrate excellent quantitative contrast of CDI, we measure the height of these variations and compare them to AFM and SEM for verification, as discussed below.

An EUV-sensitive CCD (Andor iKon-L, 2048 × 2048 pixel array, 13.5 × 13.5 μm^2 pixel size) is positioned 3.17 cm away from the sample and perpendicular to the specular reflection, resulting in a captured light NA of $\approx$ 0.4. Using a knife-edge scan, the beam size was measured at $\approx$ 12 μm in both *x*- and *y*-directions. Therefore, we chose a scanning step size of $\approx$ 3 μm in both *x*- and *y*-directions to ensure overlapping sampled areas, on an 18 × 11

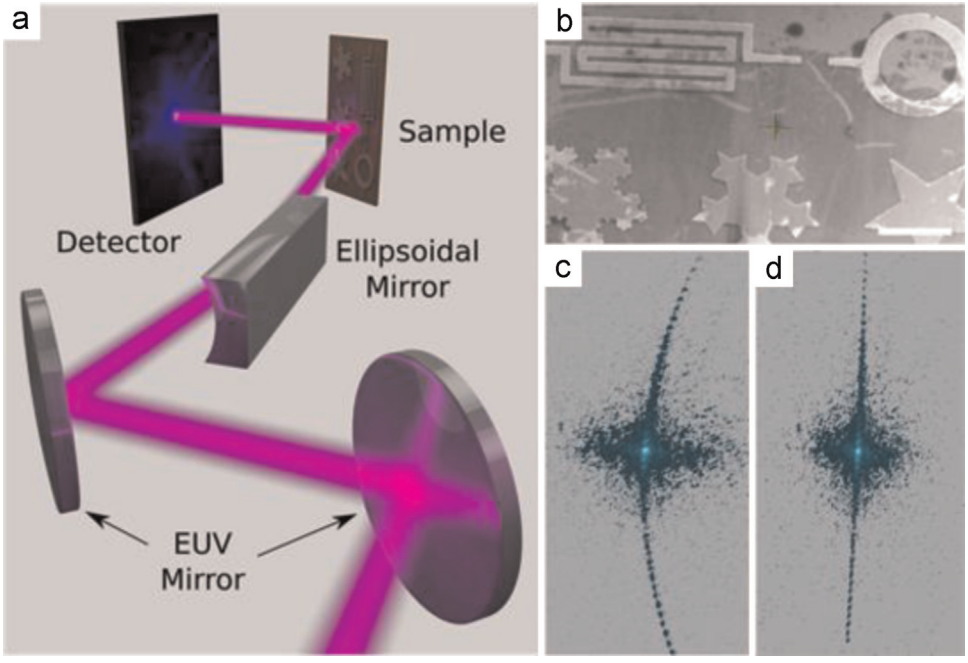

Fig. 1. Tabletop EUV ptychography. (a) Schematic of the tabletop EUV microscope. (b) SEM of the sample with a scale bar is 10 um. (c) Representative diffraction pattern from the ptychographic scan. (d) Diffraction pattern from (c) after tilted plane correction.

rectangular grid (with added random offsets up to 20% of the step size to prevent periodic artifacts in the reconstruction [32]). With each exposure of 0.1 s, and 3 accumulated exposures for each of the 198 diffraction patterns, the total exposure time was less than 1 min for the whole 65 μm × 40 μm field of view, corresponding to 44 μm^2/s exposure speed.

To account for the non-normal incidence on the sample and the high angle scattering, tilted-plane correction [22,23] must be performed to obtain the Fourier transform of the reflected exit surface wave on a linear grid of spatial frequencies. We employ tilted-plane correction for each of the 198 diffraction patterns [14]. A representative measurement is shown in Fig. 1c, while the corrected amplitude is shown in Fig. 1d. The simple effect of tilting the sample away from normal incidence results in an increased geometric field of view with decreased resolution in one direction.

As shown in Fig. 1d, the NA in the x-direction is significantly reduced compared with the y-direction, resulting in decreased resolution in x-direction. Fig. 1d shows the actual spatial frequency window we used for the reconstruction corresponding to a pixel size of 76 nm in x and 38 nm in y-direction, sampled with 512 × 1024 pixels with the same sampling frequency in both directions.

2. Discussion

We use the extended ptychographical iterative engine (ePIE) [33] with scanning position refinement [34] to retrieve the phase of the corrected diffraction patterns, which allows us to reconstruct both the illumination and the object. The reconstructed object has complex values proportional to $|r| \exp\left[i\,\varphi_r + i\,2\pi\,/\lambda\,(-2h\cos\theta_i)\right]$, where r is the complex Fresnel reflection coefficient of the sample with amplitude $|r|$ and phase φ_r, λ is the illumination wavelength, h is the height distribution of the sample, and θ_i is the angle of incidence. Due to the asymmetry in the x- and y-dimensions, we interpolated the image to upsample in the x-direction by a factor of 2. The reconstructed amplitude and phase are shown in Fig. 2a and b. For comparison, Fig. 2c shows an SEM (FEI Nova NanoSEM 630) image. We find excellent agreement between the SEM and ptychographic amplitude and phase images. Moreover, ptychography captures details of the slight surface variation that the SEM does not, and yields higher contrast images. We compare zoomed-in images from the region highlighted as a black rectangle in Fig. 2c, for ptychography amplitude and phase, SEM and AFM, in Fig. 2d–g respectively.

All images agree quite well except for very faint details-the slight height variation of the surface due to debris, circled in white and red (dashed), are clearly discernable in the ptychographic amplitude and phase images and the AFM images, but are nearly invisible to SEM. The features circled in red are completely unrecognizable in the SEM image while easily visible in the ptychographic phase and AFM images. It is evident that reflection mode CDI provides a powerful technique for surface profiling, enabling clear visualization of composition and topography with high contrast. The amplitude and phase of the reconstructed HHG beam are also shown in Fig. 2h and i. The irregular shaped beam has a size of 11 μm in x and 16 μm in y above 5% amplitude level (or 8 μm in x and 6 μm in the y direction above $1/e^2$ amplitude level). The majority of height variations within the sample area are mostly within 30 nm (except for sparse debris), and are much smaller than D/NA, justifying a model of the exit surface wave as a multiplication of the incident wave and the object response [3].

Next we present three methods to characterize the lateral resolution of our microscope: the phase retrieval transfer function (PRTF) [35–37], the modulation transfer function (MTF) (that is, the Fourier transform of the point-spread-function (PSF)), and the knife-edge test (10–90% width). PRTF is the counterpart of the MTF in coherent diffractive imaging. In conventional imaging, the MTF describes the response of an imaging system to various spatial frequencies. In coherent diffractive imaging, a phase retrieval algorithm replaces the image-forming hardware, and thus the PRTF plays a similar role to the MTF by quantifying the repeatability and accuracy of the retrieved phase as a function of spatial frequency. The PRTF evaluates the combined effect of the signal-to-noise-ratio (SNR) of the diffracted wave and systematic errors that corrupt the convergence of the retrieval algorithm. Non-normal incidence causes a significant asymmetry of the measured range of spatial frequencies in the horizontal versus vertical directions, so we evaluate the PRTF in these two directions separately; the result

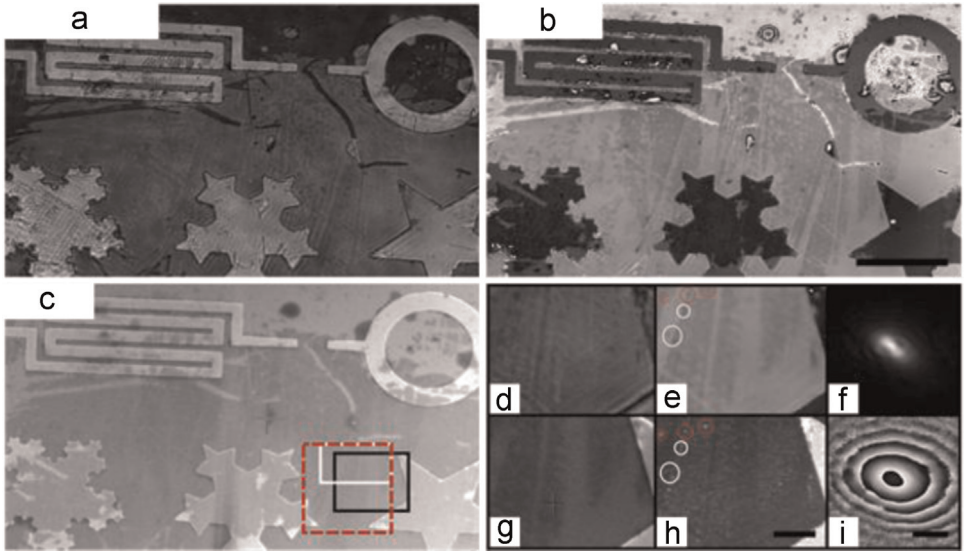

Fig. 2. High contrast full field HHG ptychographic imaging with comparison to SEM and AFM. (a) Ptychographic amplitude reconstruction. (b) Ptychographic phase reconstruction. (c) SEM image. The area enclosed in the black rectangle is zoomed in and compared with the ptychography amplitude (d), ptychography phase (e), higher resolution SEM (f), and AFM (g) with 80 nm sampling step. Areas highlighted in circles are compared in detail for the 3 techniques. (h) and (i) are the amplitude and phase of the reconstructed HHG illumination beam. Scale bar in (b) and (i) 10 μm. Scale bar in (g) 1 μm. (For interpretation of the references to color in this figure legend, the reader is referred to the web version of this article.)

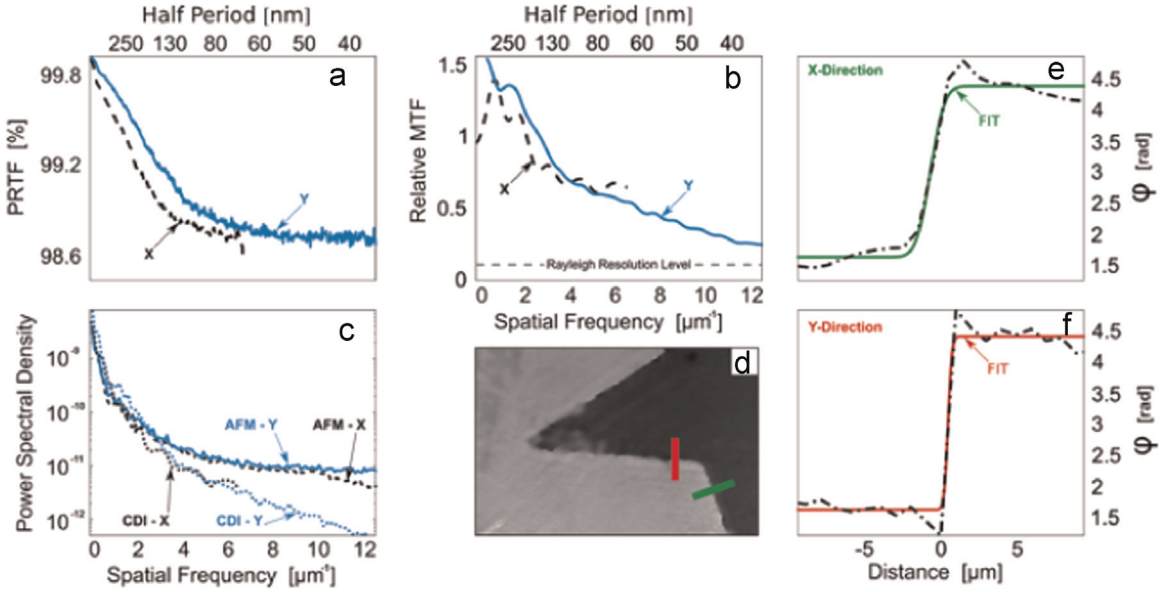

Fig. 3. Characterization of the lateral resolution. (a) Phase retrieval transfer function. (b) Relative modulation transfer function between the ptychographic phase and AFM (gray-dashed (horizontal) line: 11% contrast level corresponding to Rayleigh resolution). (c) Power spectral density. Both AFM and CDI PSDs are shown and labeled. (d) Knife edge measurement the 10–90% width of the phase reconstruction. (e) Profile measured nominally in the *x*-direction. (f) Profile measured nominally in the *y*-direction. Fits to the error function compliment, and are also shown in (e–f) as solid lines (green and red, respectively) (both R^2 values ~0.99). (For interpretation of the references to color in this figure legend, the reader is referred to the web version of this article.)

is shown in Fig. 3a. We observe that the PRTF values only slightly decrease with increasing spatial frequency in both horizontal and vertical directions and are still >0.98 at the maximum spatial frequencies. This large PRTF value is a manifestation of high SNR across the whole frequency range and accurate measurement of parameters. We conclude that the PRTF approach supports a spatial resolution of 76 nm in the horizontal direction and 38 nm in the vertical direction.

In the second characterization method, we evaluated the MTF of our CDI microscope. In the region of interest shown in Fig. 2c (red – dashed rectangle), we took a corresponding AFM measurement with a 10 nm probe diameter, and 40 nm sampling step (model: Digital Instruments Dimension 3100). Fig. 3c shows the power spectral density (PSD) of the two images from the ptychography phase and AFM measurements plotted together. By taking a square root of the ratio of the ptychographic phase and the AFM PSDs, we obtain a relative MTF: the MTF of the ptychography phase image divided the MTF of the AFM image [38]. In the absence of a much higher resolution AFM image, we are limited to claiming a relative MTF rather than absolute. However, if we can reasonably assume the AFM image has an MTF value above 50% at the highest spatial frequency (40 nm), the fact that the relative MTF is above 22% in both *x*- and *y*- directions at the maximum spatial frequency (clearly above 11%; which is the Rayleigh resolution contrast level) allows us to conclude our resolution is 76 nm horizontally and at least 40 nm vertically.

Finally, we characterize the resolution of our microscope by measuring the 10–90% width of two edges. Compared with AFM, where the image contrast comes solely from height differences, ptychography derives its contrast from the reflected complex exit surface wave. We choose two profiles nominally in the *x*- and *y*-directions (shown as green and red solid lines respectively, in Fig. 3d). The feature edges along these profiles are clean, sharp, and near the center of the ptychographic scan area avoiding insufficient overlap that can cause decreased reconstruction quality near the edges. The phase along these two profiles are shown in Fig. 3e and f respectively. We see that in the *x*-direction, the 10–90% width occurs across ~2 pixels (76 nm), and the *y*-direction rises in only 1 pixel (38 nm). The two rising edges agree well with the error function compliment (ERFC) fit that have 10–90% widths of 76 nm and 20.9 nm (<36.6 nm) respectively. (The R^2 value in either ERFC fits was ~0.99). In sum, the resolution characterized via three different approaches all support a spatial resolution of 76 nm horizontally and 38 nm vertically, corresponding to the highest measured spatial frequencies.

To determine the axial height resolution in reflection CDI, we can calculate the height from the reconstructed phase in a similar way to holography. The reconstructed phase is the sum of the geometric phase that is proportional to height, $2\pi/\lambda\,(-2h\cos\theta_i)$, and the phase of the complex reflection coefficient φ_r. Due to the lack of an absolute reference in CDI only relative phase values are accessible so when the reflecting material is monolithic, the retrieved phase is purely geometric and φ_r cancels exactly. When considering features that have different composition, φ_r is also different and must be taken into account. With some a priori information of sample composition (i.e. that the sample is composed of titanium shapes on a silicon substrate.), we generate a height map from the phase reconstruction shown in Fig. 4a. In the white rectangular area shown in Fig. 2c, the region between the stars has a homogenous composition-thus we consider only the reflection from the top, contamination layer and neglect the contribution from the silicon substrate since it has a much weaker reflection (less than 10% determined from Fig. 2a).

Visually, the ptychographic height measurement (Fig. 4d) shows good qualitative agreement with the AFM (Fig. 4e). To characterize the axial resolution of our microscope we examine surface variations highlighted in the white rectangular region, shown in Fig. 2c. It is important to note that we do not expect the lateral ptychographic resolution to be comparable with the AFM resolution in this area: because wide-angle diffraction from weakly scattering features has poor SNR, the combination of strong signal from the titanium features and detector saturation leads to a loss of transverse fidelity in this region. However, this does not affect the reconstructed height when the ratio of the feature width to the width of the PSF is much greater than unity, which is true for these surface features. On the other hand, this condition is not met for the very fine debris apparent in the AFM image.

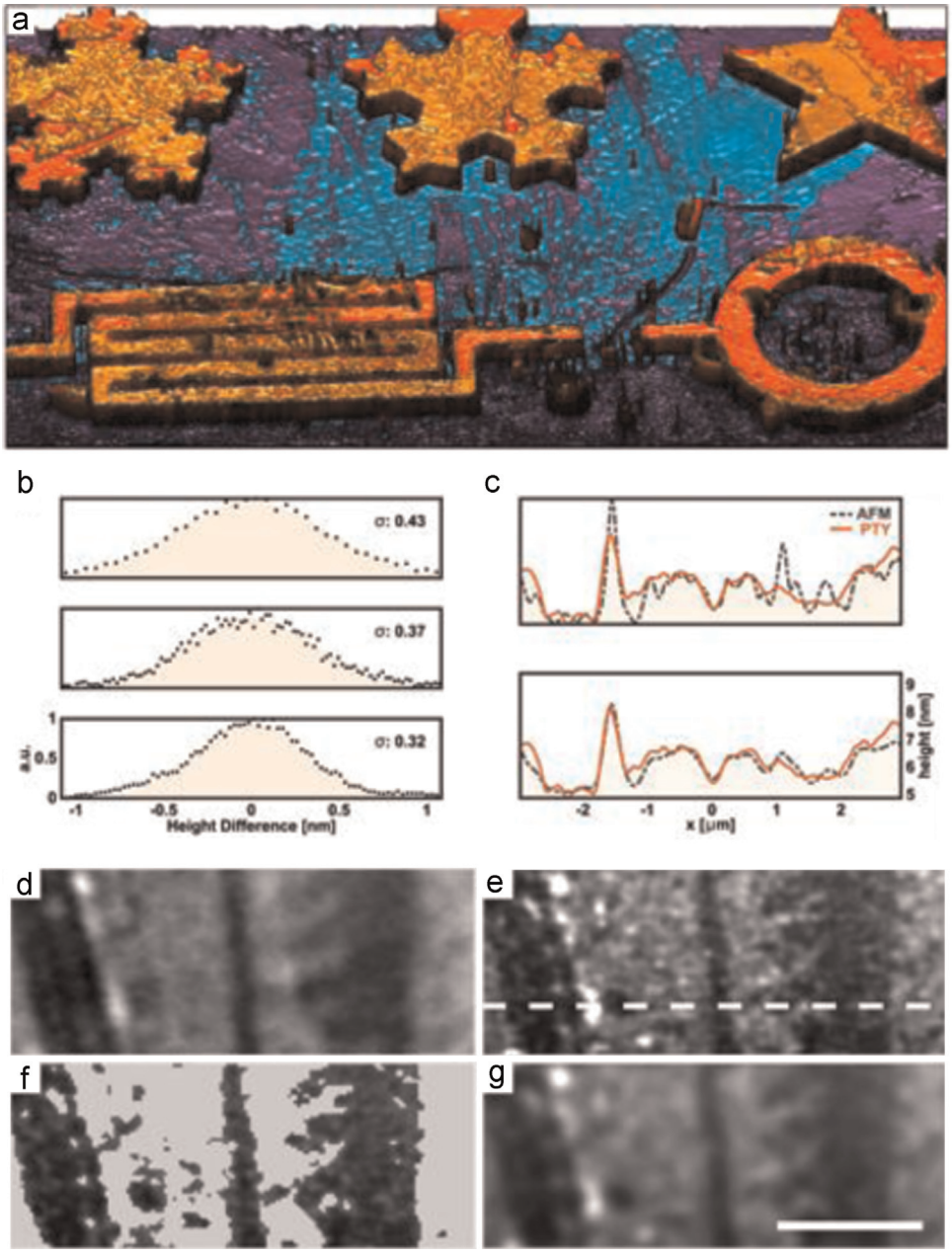

Fig. 4. Extracting the height and axial resolution. (a) Three-dimensional rendering of surface features imaged by ptychographic CDI. (b) Histograms of the height differences measured by ptychography and AFM. The top panel includes no filtering (comparing (d)–(e) directly). The middle panel uses a histogram filter to remove values outside the trench features (comparing (d)–(f)). The bottom panel used a Gaussian-PSF to smooth fine debris in the AFM (comparing (d)–(g)). The *y*-axis is shared between all panels in (b). Scale bar, 2 μm shared with (d–g). (c) Comparative profiles taken along the dashed (white) line in (e). The top panel compares (d)–(e). The bottom panel compares (d)–(g). The *y*-axis is shared between all panels in (c). After smoothing, the 2-σ (95% confidence interval) width, in height difference is ~6 Å.

In order to more accurately compare the height variations measured by either AFM or ptychography we apply two filters. First, we simply remove points outside the wide, trench features using a histogram filter in both the AFM and ptychographic images, shown in Fig. 4c. Second, we convolve a Gaussian PSF ($\sigma=70$ nm) with the AFM measurement. The width of the Gaussian PSF was chosen to minimize the overall error between the AFM and ptychographic reconstruction. The results of both the histogram filtering and PSF-filtering are shown in Fig. 4f and g; these are compared against the ptychographic height map in Fig. 4d. The three panels shown in Fig. 4b are a histogram of the height difference between the ptychographic reconstruction and the AFM image for different filters.

The top-most histogram and corresponding Gaussian fit with reported width $\sigma=4.3$ Å compares the unfiltered AFM (Fig. 4e) directly to the ptychographic reconstruction. The center histogram and corresponding Gaussian fit with reported width, $\sigma=3.7$ Å compares the histogram filtered, ptychographic height map to the histogram filtered AFM (Fig. 4f). The bottom-most histogram and corresponding Gaussian fit with reported width, $\sigma=3.2$ Å compares the ptychographic height map to the Gaussian-PSF filtered AFM image (Fig. 4g). Two representative profiles are shown in Fig. 4c corresponding to the white dashed line in Fig. 4e. In Fig. 4c the top-most panel is a direct comparison between the unfiltered AFM and ptychographic height reconstruction. The bottom-most panel compares the PSF-filtered AFM with the ptychographic reconstruction. The three comparisons (Fig. 4b) are in good relative agreement however; the fact that both filtered versions of the AFM image show lower relative difference results from the omission of

spurious debris which could not be reconstruct with high fidelity by CDI.

3. Conclusion

We have demonstrated tabletop HHG ptychographic coherent imaging of a surface with unprecedented fidelity, comparing favorably with well-established techniques such as SEM and AFM. We achieve lateral resolutions of 40 nm × 80 nm horizontally, as well as sub-nanometer axial precision. EUV reflection provides a powerful imaging contrast mechanism; it has composition sensitivity unlike AFM and improved contrast compared to SEM. Additionally, ptychography CDI does not require the sample to be conductive as in conventional SEM. Instead of serial, point-by-point scanning, EUV ptychography employs a wide field of view at every scan position, significantly decreasing the time for scanning, and making source flux the only practical limit for high volume imaging. The increase of the imaging speed makes this method attractive for real applications involving large-area imaging, such as semiconductor inspection. In contrast to AFM, this microscopy provides a long working distance—in this work, only limited by sample-detector distance (31.66 mm). HHG ptychographic CDI also compares favorably with the SEM in terms of damage—the SEM often left surface contamination and charge after scanning.

The cumulative exposure time for this technique is quite comparable to an SEM (in our case, ~20 × shorter than the total acquisition time of the SEM). However, the total acquisition time for the exposure was quite slow (~1 h) in this prototype instrument, primarily due to the slow readout of the CCD and settling time of the stages. Fast-readout CCD technology does exist and can bring readout times down significantly and continuous scanning modes are possible [39,40]. Image reconstruction using a GPU currently takes an intermediate time (~2–60 min) depending on desired fidelity, but likely can be performed in near real-time with further optimization and upgraded hardware.

The resolution we achieve can be improved by using shorter HHG wavelengths, including the technologically important 13.5 nm. Additionally, by taking a second data set with the sample rotated at 90°, we can ensure a high resolution of 1.3λ in both *x*- and *y*-directions. Furthermore, substantial increases in imaging NA are possible using larger or multiple CCDs, or a CCD with a through-aperture that allows closer sample placement. Combined with the femtosecond pulse duration naturally associated with HHG sources, HHG CDI can combine ultrahigh spatial and temporal resolution, to probe the fastest dynamic processes relevant to function at the nanoscale.

4. Methods

4.1. Image reconstructions

To obtain the initial guess of the probe (beam), we measured the far-field beam reflected from a flat, featureless area of the sample substrate. We assume a quadratic phase with *x*- and *y*-radius taken as the distance from the measured *x*- and *y*-focus to the detector [14]. We perform tilted plane correction on the beam field guess and then back-propagate to the sample plane to produce the initial probe guess. We use a constant value for the initial object guess. We use the ePIE [33] algorithm, and update only the object in the first two iterations. In the following 30 iterations, we update both the object and the probe. For the next 50 iterations, we update the object with position refinement [34]. For the next 600 iterations, we update the object and the probe and use position refinement. We finish the reconstruction procedure with 150 iterations of object update only. Our ePIE algorithm is implemented in C++, with OpenCV library support, on an NVIDIA Tesla K40c GPU. Each iteration takes, at most 4.6 s (with probe, object update and position refinement on) for all of the 198 diffraction patterns, each of which has a grid size of 512 by 1024. Dominant features become clear at less than 32 iterations (2.5 min), and all 832 iterations take less than one hour.

4.2. Phase retrieval transfer function

PRTF is calculated as:

$$\mathrm{PRTF}(f_{1D}) = \frac{\left\langle \left\langle \left| \left\langle E_{i,j}^{\mathrm{rec.}}(f_x, f_y) \right\rangle_j \right| \right\rangle_i \right\rangle_{1D}}{\left\langle \left\langle \left| E_i^{\mathrm{meas.}}(f_x, f_y) \right| \right\rangle_i \right\rangle_{1D}}$$

where $|E_i^{\mathrm{meas.}}(f_x, f_y)|$ is the magnitude of the measured electric field on the detector corresponding to spatial frequency (f_x, f_y) and the *i*th scan position, $E_{i,j}^{\mathrm{rec.}}(f_x, f_y)$ is the reconstructed electric field at the *j*th iteration and the *i*th scan position, corresponding to spatial frequency (f_x, f_y), $\langle\,\rangle_j$ and $\langle\,\rangle_i$ are averages over iterations and scan positions respectively, $\langle\,\rangle_{1D}$ means average over one direction to transform a 2-dimensional signal to a 1-dimensional signal. We average over f_y when evaluating $\mathrm{PRTF}(|f_x|)$, and over f_x when evaluating PRTF $|f_y|$. We started with the 832nd iteration, which we considered the converged reconstruction. We averaged 100 iterations during which time only the object was updated.

Acknowledgments

The authors gratefully acknowledge support from the Defense Advanced Research Projects Agency (DARPA) (DARPA-BAA-12-63), the National Science Foundation COSI IGERT 0801680, ERC in EUV Science and Technology 0310717, and the Semiconductor Research Corporation (SRC) (2013-OJ-2443). The authors also acknowledge C. Porter for insightful discussion, commentary and graphical advice.

References

[1] H. Faulkner, J. Rodenburg, Movable aperture lensless transmission microscopy: a novel phase retrieval algorithm, Phys. Rev. Lett. 93 (2004) 023903.
[2] J. Rodenburg, et al., Hard-x-ray lensless imaging of extended objects, Phys. Rev. Lett. 98 (2007) 034801.
[3] P. Thibault, et al., High-resolution scanning x-ray diffraction microscopy, Science 321 (2008) 379–382.
[4] A. Rundquist, et al., Phase-matched generation of coherent soft x-rays, Science 280 (1998) 1412–1415.
[5] R.A. Bartels, et al., Generation of spatially coherent light at extreme ultraviolet wavelengths, Science 297 (2002) 376–378.
[6] P.B. Corkum, Plasma perspective on strong-field multiphoton ionization, Phys. Rev. Lett. 71 (1993) 1994–1997.
[7] T. Popmintchev, et al., Extended phase matching of high harmonics driven by mid-infrared light, Opt. Lett. 33 (2008) 2128–2130.
[8] M.-C. Chen, et al., Bright, coherent, ultrafast soft x-ray harmonics spanning the water window from a tabletop light source, Phys. Rev. Lett. 105 (2010) 173901.
[9] T. Popmintchev, et al., Bright coherent ultrahigh harmonics in the keV x-ray regime from mid-infrared femtosecond lasers, Science 336 (2012) 1287–1291.
[10] T. Popmintchev, M.-C. Chen, P. Arpin, M.M. Murnane, H.C. Kapteyn, The attosecond nonlinear optics of bright coherent x-ray generation, Nat. Photonics 4 (2010) 822–832.
[11] K. Midorikawa, High-order harmonic generation and attosecond science, Jpn. J. Appl. Phys. 50 (2011) 1–12.
[12] R.L. Sandberg, et al., Lensless diffractive imaging using tabletop coherent high-harmonic soft-x-ray beams, Phys. Rev. Lett. 99 (2007) 1–4.
[13] M.D. Seaberg, et al., Ultrahigh 22 nm resolution coherent diffractive imaging using a desktop 13 nm high harmonic source, Opt. Express 19 (2011) 22470–22479.
[14] B. Zhang, et al., Full field tabletop EUV coherent diffractive imaging in a

transmission geometry, Opt. Express 21 (2013) 839–843.
[15] a. Ravasio, et al., Single-shot diffractive imaging with a table-top femtosecond soft x-ray laser-harmonics source, Phys. Rev. Lett. 103 (2009) 28104.
[16] M. Zürch, C. Kern, C. Spielmann, XUV coherent diffraction imaging in reflection geometry with low numerical aperture, Opt. Express 21 (2013) 21131–21147.
[17] R.A. Dilanian, et al., Diffractive imaging using a polychromatic high-harmonic generation soft-x-ray source, J. Appl. Phys. 106 (2009) 023110.
[18] B. Zhang et al., Quantitative tabletop coherent diffraction imaging microscope for EUV lithography mask inspection, in: Proceedings of SPIE, vol. 9050, 2014, pp. 90501D–1.
[19] T. Harada, J. Kishimoto, T. Watanabe, H. Kinoshita, D.G. Lee, Mask observation results using a coherent extreme ultraviolet scattering microscope at NewSUBARU, J. Vac. Sci. Technol. B Microelectron. Nanometer Struct. 27 (2009) 3203.
[20] S. Marathe, et al., Coherent diffraction surface imaging in reflection geometry, Opt. Express 18 (2010) 7253–7262.
[21] S. Roy, et al., Lensless x-ray imaging in reflection geometry, Nat. Photonics 5 (2011) 243–245.
[22] D.F. Gardner, et al., High numerical aperture reflection mode coherent diffraction microscopy using off-axis apertured illumination, Opt. Express 20 (2012) 19050.
[23] T. Sun, Z. Jiang, J. Strzalka, L. Ocola, J. Wang, Three-dimensional coherent x-ray surface scattering imaging near total external reflection, Nat. Photonics 6 (2012) 586–590.
[24] M.D. Seaberg, et al., Tabletop nanometer extreme ultraviolet imaging in an extended reflection mode using coherent Fresnel ptychography, Optica 1 (2014) 39.
[25] I. Robinson, et al., Coherent x-ray diffraction imaging of silicon oxide growth, Phys. Rev. B 60 (1999) 9965–9972.
[26] M. Knoll, Aufladepotentiel und sekundäremission elektronenbestrahlter körper, Z. Tech. Phys. 16 (1935) 467–475.
[27] M. Von Ardenne, Das elektronen-rastermikroskop. Theoretische grundlagen, Z. Phys. 109 (1938) 553–572.
[28] M. von Ardenne, Das elektronen-rastermikroskop. Praktische ausführung, Z. Tech. Phys. 19 (1938) 407–416.
[29] G. Binnig, C.F. Quate, Atomic force microscope, Phys. Rev. Lett. 56 (1986) 930–933.
[30] F. Brizuela, et al., Microscopy of extreme ultraviolet lithography masks with 132 nm tabletop laser illumination, Opt. Lett. 34 (2009) 271.
[31] P.P. Naulleau, et al., Electro-optical system for scanning microscopy of extreme ultraviolet masks with a high harmonic generation source, Opt. Express 22 (2014) 20144.
[32] P. Thibault, M. Dierolf, O. Bunk, A. Menzel, F. Pfeiffer, Probe retrieval in ptychographic coherent diffractive imaging, Ultramicroscopy 109 (2009) 338–343.
[33] A.M. Maiden, J.M. Rodenburg, An improved ptychographical phase retrieval algorithm for diffractive imaging, Ultramicroscopy 109 (2009) 1256–1262.
[34] F. Zhang, et al., Translation position determination in ptychographic coherent diffraction imaging, Opt. Express 21 (2013) 13592–13606.
[35] D. Shapiro, et al., Biological imaging by soft x-ray diffraction microscopy, Proc. Natl. Acad. Sci. U.S.A. 102 (2005) 15343–15346.
[36] H.N. Chapman, et al., High-resolution ab initio three-dimensional x-ray diffraction microscopy, JOSA A 23 (2006) 1179–1200.
[37] R.N. Wilke, et al., Hard x-ray imaging of bacterial cells: nano-diffraction and ptychographic reconstruction, Opt. Express 20 (2012) 19232.
[38] C. Jacobsen, et al., Diffraction-limited imaging in a scanning transmission x-ray microscope, Opt. Commun. 86 (1991) 351–364.
[39] D. Doering, et al., Development of a compact fast CCD camera and resonant soft x-ray scattering endstation for time-resolved pump-probe experiments, Rev. Sci. Instrum. 82 (2011) 073303.
[40] J.N. Clark, X. Huang, R.J. Harder, I.K. Robinson, Continuous scanning mode for ptychography, Opt. Lett. 39 (2014) 6066–6069.